energy&fuels

pubs.acs.org/EF

Article

Modeling Biomass Particle Evolution at Pyrolysis Conditions Considering Shrinkage and Chemical Kinetics with Conjugate Heat Transfer

Yongsuk Cho and Song-Charng Kong*

Cite This: *Energy Fuels* 2023, 37, 5926–5941

Read Online

ACCESS | Metrics & More | Article Recommendations

ABSTRACT: Biomass pyrolysis is an attractive method to produce renewable biofuel in a short time scale. This paper discusses a computational study considering particle shrinkage and reaction kinetics to characterize biomass particle evolution under pyrolysis conditions. A representative elementary volume (REV) scale simulation was conducted in three dimensions to resolve the gas and solid domains. The interface was modeled using the conjugated heat transfer (CHT) and the adapted partially saturated method (PSM) in the lattice Boltzmann (LB) framework. A sufficient gas thickness was considered to simulate the interface physics, such as the thermal boundary layer and product gas outflux. The current simulation was validated using three different experiments. The particle conversion time, temperature, and shrinkage were well predicted. A parametric study investigated the effect of different modeling approaches and operating conditions. Results show that the internal heat transfer is affected by the particle size, inlet gas velocity, reactor temperature, and geometry. The Fourier number decreases to a nearly constant value as the particle size increases. The Péclet number increases linearly with the reactor temperature. Sub-particle scale simulation results reveal that the CHT model and permeability need to be considered when simulating gaseous product efflux out of the biomass particle. Three regimes are identified based on the particle permeability: diffusion-limited, mixed, and advection-limited. The gaseous product efflux delays the overall conversion in the mixed regime. A modified heat transfer coefficient is formulated based on the current numerical study.

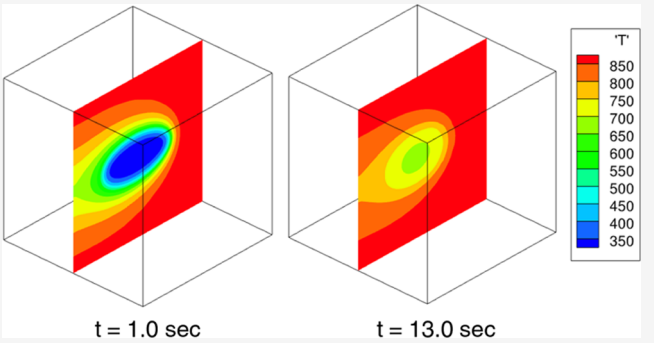

1. INTRODUCTION

Nonfood biomass can be converted to energy products via proper methods, such as pyrolysis and fermentation. The so-called second-generation biofuel has the potential to enhance the overall renewable energy portfolio without encountering the controversy of food versus fuel.[1] The importance of such bioenergy cannot be underestimated due to the need for transportation, national security, and other demands that electrification is impossible to meet.[2] The present paper will be focused on pyrolysis technology, an effective way to convert biomass to fuel.

Pyrolysis is a thermochemical conversion process of biomass into energy products by breaking down complex organic structures in an oxygen-deficient environment. Lignocellulosic biomass mainly comprises three organic compounds: cellulose, hemicellulose, and lignin, in addition to a small portion of extractives and minerals.[3] Depending on the composition of these materials, biomass has different thermophysical properties. As a result of pyrolysis reactions, volatile gas and biochar are produced. The emitted volatiles can be categorized into noncondensable syngas and condensable tar which leads to bio-oil.[4] Bio-oil can be further upgraded to transportation fuels. Biochar is a solid carbon residue that can be combusted as a solid fuel or buried into the ground to achieve a so-called negative carbon economy (by capturing carbon from the atmosphere via vegetation) and be used as an agronomic asset. Fast pyrolysis is attractive due to its rapid conversion speed.[5] In recent decades, pilot plants utilizing biomass fast pyrolysis have been built. However, commercial operations remain a challenge. A fundamental understanding of the complex fast pyrolysis process is needed.

Fast pyrolysis involves various scales of the physicochemical phenomena ranging from the reactor scale to the microscopic sub-particle scale. These multiscale phenomena are interrelated.[6] It is important to formulate a macroscopic model by

Received: November 16, 2022
Revised: March 16, 2023
Published: March 30, 2023

incorporating microscopic effects for accurate modeling. The macroscopic process involves the multiphase flow of solid biomass particles and inert gas (mainly nitrogen or argon) with heat transfer and chemical reactions. Experimental results[7−11] provide important insights into biomass conversion, product yield, and reaction time (residence time). However, the limited accessibility in experiments has hindered the detailed understanding of particle scale biomass evolution. Numerical modeling can be used as a tool to help understand the problem.

One- and two-dimensional (2D) models[7,8] were formulated for solving the mass and energy transport equations. In these models, the heat transfer coefficients were empirically modeled. Lu et al.[12] simulated the momentum transport of both gas and solid phases. The convection heat transfer coefficient was modeled based on evolving pore diameter. Numerous modeling approaches have been proposed, such as those considering a detailed particle morphology in three dimensions[13] and focusing on anisotropic heat transfer with the pyrolytic product outflux.[14] Based on the Stefan correlation, a modified convection heat transfer coefficient was used to incorporate the surface mass flux.[15]

The heat transfer around the particle surface is governed by the conjugate heat transfer (CHT) between the solid and gas phases. When biomass particles at room temperature are injected into a pyrolytic reactor, the gas temperature near the particle surface decreases rapidly due to the low thermal capacity of the gas phase. Because of the porous nature of biomass, the convection heat transfer coefficient changes dynamically. In addition, the thermal boundary layer thickness changes with particle evolution due to the changing temperature gradient. The above macroscopic effects will change the pyrolysis regime[16] and must be considered in the numerical model. By directly resolving the surface normal mass flux of the three-dimensional (3D) geometries, the conjugate heat transfer model can be a useful tool for investigating biomass heat transfer.

A biomass particle is intrinsically an anisotropic porous material at the microscopic level. During fast pyrolysis, the porosity of biomass particles changes dynamically.[17,18] It is also known that biomass has different thermal conductivities in different directions.[19] The composition and weight of the particle evolve during the pyrolytic reaction. Depending on the reactor temperature, the pore diameter can change significantly,[18,20] affecting heat and mass transfer as well as the shrinkage of the biomass particle. The particle shrinkage occurs because of the breakdown of biomass molecular structure. The shrinkage decreases the particle Reynolds number, altering momentum and heat transfer and affecting the overall particle conversion time. In most studies, empirical formulas are adopted, considering a linear relationship between shrinkage and conversion ratio[21−24] and assuming the constant porosity.[25] However, the conversion ratio is not the sole factor. The overall particle shrinkage is less when the reactor temperature is higher.[20,26] This is due to the increase in the particle pore diameter. A more accurate model should include the effects of the reactor temperature.

The lattice Boltzmann (LB) method[27] has been used to study biomass particle fast pyrolysis.[28,29] The LB method describes the physical properties of a fluid using discrete distribution functions originating from the Boltzmann equation. With the advantages of robust parallel computation and ease of posing complex boundary implementation, the LB method has been actively developed for simulating various flow problems. It is also a good candidate to tackle the multiscale phenomena of biomass pyrolysis. Biomass pyrolysis involves unsteady multiphase thermal flows, reactive flows, and flows through porous media. Various types of conjugate heat transfer (CHT) models have been developed to overcome the temperature (T) and temperature flux (q) mismatch in the conventional convection-diffusion equation of the thermal LB model when solving heterogeneous media (i.e., $T_{gas} = T_{solid}$ and $q_{gas} = q_{solid}$). Most of them fall into three categories: (1) interface schemes,[30−32] (2) source term treatments,[33−35] and (3) new thermal LB formulations.[36−38] All three types of models can simulate the unsteady CHT with reasonable accuracy. However, the third scheme used in the present study is a strictly LB-style formulation using one stencil compared to the first two schemes. Thus, no neighboring lattice information is needed. The numerical stability of the third scheme is higher when experiencing high-density ratio heat transfer, i.e., the CHT between the gas and solid, as there is no need to add another boundary condition or source term, which is the primary cause of numerical instabilities.[39]

To accurately simulate reactive flows, capturing the density fluctuation induced by temperature and concentration differences is important. A low Mach number assumption (LMNA) is usually adopted to simulate reactive flows in the incompressible framework. Various reactive thermal flow models are introduced based on the double distribution function approach;[40] these models can consider the temperature-based method[41] or the total energy-based method.[42−44] Lastly, there are two types of LB models for simulating porous media flows. Taking advantage of a simple boundary condition implementation, one can directly resolve the porous structure at the pore scale.[45] Some recent studies use the representative elementary volume (REV) scale LB model. The REV scale simulation uses a larger domain than the pore scale simulation, and the volume-averaged transport properties at each lattice are of interest.[46] Recently, Guo and Zhao proposed a generalized REV scale LB model[47] to simulate convection heat transfer.[48] The model can simulate unsteady problems with variable porosity and is applicable to biomass pyrolysis if the reaction and mass transfer models are correctly posed. Furthermore, a more complex model to predict biomass pyrolysis can be derived by incorporating anisotropy of biomass with the aid of the multiple-relaxation-time (MRT) LB model.[49] Compared to the single-relaxation-time LB model, the MRT method conserves transport properties when the relaxation time of one direction is different from others.

The LB method presented in this paper considers several important aspects of physics involved in biomass pyrolysis. It bridges different length scales by considering biomass shrinkage and porous media effects in the current particle simulation. The following sections will describe the numerical method and results. The mesoscopic LB model is presented, from which the macroscopic equations are retrieved. A shrinkage model is proposed and integrated into the current LB model with a proper interface treatment between the porous biomass particle and the surrounding gas. The Results and Discussion section includes the model validation using three different experiments, followed by a series of parametric studies. Based on these observations, a new heat transfer coefficient for the evolving biomass particle is formulated and compared with those in the literature.

2. NUMERICAL METHOD

Governing equations with proper physical modeling are solved to resolve the particle-level biomass pyrolysis in three

https://doi.org/10.1021/acs.energyfuels.2c03892
Energy Fuels 2023, 37, 5926−5941

dimensions. The LB equations are formulated in a way to achieve efficient numerical simulations.

2.1. Governing Equations and Physical Model. The REV scale porous model is formulated for simulating the momentum transport to resolve the gas flow inside the biomass particle. The pressure work and viscous dissipation are neglected. A set of conservation equations are formulated as

$$\frac{\partial(\varepsilon\rho)}{\partial t} + \nabla\cdot(\rho\mathbf{u}) = 0$$
$$\frac{\partial(\rho\mathbf{u})}{\partial t} + \nabla\cdot\left(\frac{\rho\mathbf{u}\mathbf{u}}{\varepsilon}\right) = -\nabla(\varepsilon p) + \nabla\cdot(\rho\nu_e\nabla\mathbf{u}) + \rho\mathbf{F}$$
$$\frac{\partial(\overline{\rho c_p}T)}{\partial t} + \nabla\cdot(\rho c_p T\mathbf{u}) = \nabla\cdot(\rho c_p\alpha_e\nabla T) + Q$$
$$\frac{\partial\rho Y_i}{\partial t} + \nabla\cdot(\rho Y_i\mathbf{u}) = \nabla\cdot(\rho D_i\nabla Y_i) + R_i \quad (1)$$

where ρ, $\mathbf{u}$, T, and Y_i are, respectively, the volume-averaged gas density, velocity vector, temperature, and species concentration of component i (e.g., syngas and tar). In the momentum equation, ε and ν_e represent the porosity and effective viscosity, respectively. The porosity is determined as $\varepsilon = 1 - \frac{\rho_{solid}}{\rho_w}(1 - \varepsilon_w)$ where ρ_{solid} is the time-varying solid density and ρ_w and ε_w represent the initial biomass density and porosity, respectively. $\overline{\rho c_p}$ is the local thermal capacity of interest. It is defined as $(\rho c)_{solid}$ for the solid phase and $(\rho c_p)_{gas}$ for the gas phase. The effective thermal diffusivity, α_e, is formulated as $\kappa_e/(\rho c_p)_{gas}$ so that the energy equation can resolve the porous biomass particle by incorporating the interior radiation between the solid and gas phases. κ_e is the effective conductivity.[8,29] In the case of the solid phase, it is written as

$$\kappa_e = (1 - \eta)\kappa_w + \eta\kappa_{char} + \varepsilon\kappa_{gas} + 13.5\alpha T^3 d \quad (2)$$

where α and d are the Stefan−Boltzmann constant and the pore diameter, respectively, and η is the conversion extent of pyrolysis defined as $\eta = 1 - \frac{\rho_{solid} - \rho_{char}}{\rho_w}$. The thermal conductivities of each component depend on the temperature and are shown in Tables 2 and 3. D is the binary diffusion coefficient of the species of interest to the inert gas. R, Q, and $\mathbf{F}$ are the source or sink terms of each transport equation. R and Q are mainly due to the pyrolytic reaction, and $\mathbf{F}$ is given as

$$\mathbf{F} = -\frac{\varepsilon\nu_f}{K}\mathbf{u} - \frac{\varepsilon F_\varepsilon}{\sqrt{K}}|\mathbf{u}|\mathbf{u} - \varepsilon\mathbf{a} \quad (3)$$

where the first two terms are related to the drag inside of the particle and are removed when solving the gas phase. The first term is the Darcy model to resolve the linear drag, and the second is the Forchheimer term to cope with the nonlinear drag. The last term is the body force (i.e., gravity) of the gas phase. ν_f and K are the viscosity of gas and the permeability of biomass particle, respectively. Based on the experiment,[46] the geometric function F_ε and permeability K are formulated as

$$F_\varepsilon = \frac{1.75}{\sqrt{150\varepsilon^3}},\ K = \frac{\varepsilon^3 d^2}{150(1 - \varepsilon)^2} \quad (4)$$

The multistep pyrolytic reaction model is used in this study to simulate hardwood types of biomaterials. A more sophisticated kinetics model[50] is available in the literature in which different types of biomass (i.e., hardwood, softwood, and grass) are handled separately, but different particle shrinkage mechanisms will be required. Figure 1 shows the reaction pathways of three

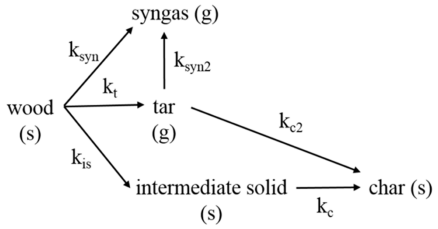

Figure 1. Reaction pathways considered in the current simulation.

competing products: syngas, tar, and char, based on the Arrhenius reaction rate ($k_i = A_i\, e^{-E_i/RT}$). The corresponding kinetic parameters and heat of reaction are provided in Table 1. The syngas and tar are assumed to be in the gas phase due to the high reactor temperature, and the char and intermediate (activated) solids are considered in the solid phase. The resultant source and sink terms in the mass, temperature, and species equations are determined and added at each time-step.[8,29]

$$\text{virgin wood: } \frac{\partial\rho_b}{\partial t} = R_b = -(k_t + k_{syn} + k_{is})\rho_b \quad (5)$$

$$\text{intermediate solid: } \frac{\partial\rho_{is}}{\partial t} = R_{is} = k_{is}\rho_b - k_c\rho_{is} \quad (6)$$

$$\text{char: } \frac{\partial\rho_c}{\partial t} = R_c = k_c\rho_{is} + k_{c2}\rho_t \quad (7)$$

$$\text{tar: } \frac{\partial\rho_t}{\partial t} + \nabla\cdot(\rho_t\mathbf{u}) = R_t = k_t\rho_b - (k_{c2} + k_{syn2})\rho_t \quad (8)$$

$$\text{syngas: } \frac{\partial\rho_{syn}}{\partial t} + \nabla\cdot(\rho_{syn}\mathbf{u}) = R_{syn} = k_{syn}\rho_b + k_{syn2}\rho_t \quad (9)$$

$$Q = -(k_t\Delta h_t + k_{syn}\Delta h_{syn} + k_{is}\Delta h_{is})\rho_b - k_c\Delta h_c\rho_{is} - (k_{c2}\Delta h_{c2} + k_{syn2}\Delta h_{syn2})\rho_t \quad (10)$$

Lastly, the interface between the porous solid and gas phase must follow the conjugated condition

$$\begin{cases} T_{gas} = T_{solid} \\ \mathbf{n}[-\kappa_{gas}\nabla T + (\rho c_p)_{gas}\mathbf{u}T]_{gas} \\ \quad = \mathbf{n}[-\kappa_{solid}\nabla T + (\rho c_p)_{gas}\mathbf{u}T]_{solid} \end{cases} \quad (11)$$

where $\mathbf{n}$ is the surface normal component vector. The terms in parentheses are the conduction and advection terms, respectively. It should be mentioned that the advection term should not be neglected due to the porous solid. The thermal LB formula in the next section satisfies the conjugated condition without the need to pose any interface treatment.

2.2. Lattice Boltzmann Method. The LB equation with the MRT collision model is adopted to simulate biomass pyrolysis. The MRT model has better numerical stability than the single relaxation model, with a slight compromise in the overall computation time. In addition, the MRT model can handle anisotropic conditions as it can impose different

https://doi.org/10.1021/acs.energyfuels.2c03892
Energy Fuels 2023, 37, 5926−5941

Table 1. Kinetic Parameters and Heat of Reaction[8]

reaction	k_t	k_{syn}	k_{is}	k_c	k_{c2}	k_{syn2}
A_i (s^{-1})	1.08×10^{10}	4.38×10^{9}	3.75×10^{6}	1.38×10^{10}	1.0×10^{5}	4.28×10^{6}
E_i (J mol^{-1})	148,000	152,700	111,700	161,000	108,000	108,000
Δh_i (J kg^{-1})	80,000	80,000	80,000	−300,000	−42,000	−42,000

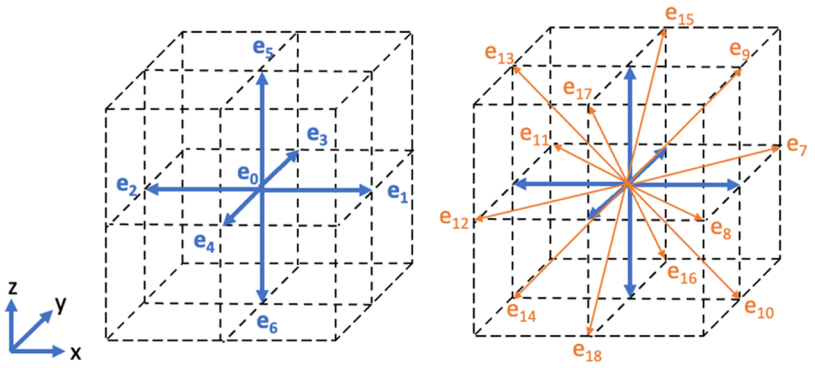

Figure 2. Lattice discrete velocities for D3Q7 (left) and D3Q19 (right) models used in the current study.

relaxation rates on each direction of interest. An LB equation has a variety of discrete velocity sets in two- and three-dimensional simulations. It is denoted as *DdQq*, where *d* stands for dimensions, and *q* is the number of discrete velocities, $\{\mathbf{e}I = 0, 1, \cdots, q-1\}$. The D3Q19 lattice configuration is used for the momentum transfer, and the D3Q7 model is used for energy and concentration equations. Figure 2 shows different types of discrete models adopted for conservation equations. The LB-MRT model is described as,

$$f_i(\mathbf{x} + \delta_t\mathbf{e}, t + \delta_t) - f_i(\mathbf{x}, t) = -\mathbf{M}^{-1}\mathbf{S}_f[\mathbf{m}(\mathbf{x}, t) - \mathbf{m}^{eq}(\mathbf{x}, t)] + \delta_t F_i \quad (12)$$

$$g_i(\mathbf{x} + \delta_t\mathbf{e}, t + \delta_t) - g_i(\mathbf{x}, t) = -\mathbf{N}^{-1}\mathbf{S}_g[\mathbf{n}(\mathbf{x}, t) - \mathbf{n}^{eq}(\mathbf{x}, t)] + \delta_t Q_i \quad (13)$$

where f and g stand for the density and energy distribution functions, respectively. These distribution functions evolve over space and time after having them relaxed in the moment space of each discrete lattice by equilibrium moment matrices $\mathbf{m}^{eq}$, $\mathbf{n}^{eq}$. The species distribution function, h_i, is not shown here due to its similar formulation in the energy equation. Once the heat capacity ratio, σ in eq 17, becomes 1, the distribution function solves the general form of the convection-diffusion equation for species transport. The operator splitting scheme[51,52] considers the source and sink terms in the MRT framework. By doing so, the source for the mass and momentum can be applied separately in the density distribution function.

The distribution functions f, g are converted into the moment space and vice versa by executing moment matrices $\mathbf{M}$, $\mathbf{N}$ multiplication.

$$\mathbf{m} = \mathbf{M}\cdot f,\ f = \mathbf{M}^{-1}\cdot\mathbf{m} \quad (14)$$

$$\mathbf{n} = \mathbf{N}\cdot g,\ g = \mathbf{N}^{-1}\cdot\mathbf{n} \quad (15)$$

The moment matrices for D3Q7 and D3Q19 can be found in the literature.[39] The equilibrium distribution functions are formulated as[38,41]

$$f_0^{eq} = \rho\left[1 - \frac{2T}{3}\sum_k \frac{Y_k}{W_k} - \frac{|\mathbf{u}|^2}{6\varepsilon c_s^2}\right]$$

$$f_{1-6}^{eq} = \frac{1}{18}\rho\left[T\sum_k \frac{Y_k}{W_k} + \frac{\mathbf{e}_i\cdot\mathbf{u}}{c_s^2} + \frac{(\mathbf{e}_i\cdot\mathbf{u})^2}{2\varepsilon c_s^4} - \frac{|\mathbf{u}|^2}{2\varepsilon c_s^2}\right]$$

$$f_{7-18}^{eq} = \frac{1}{36}\rho\left[T\sum_k \frac{Y_k}{W_k} + \frac{\mathbf{e}_i\cdot\mathbf{u}}{c_s^2} + \frac{(\mathbf{e}_i\cdot\mathbf{u})^2}{2\varepsilon c_s^4} - \frac{|\mathbf{u}|^2}{2\varepsilon c_s^2}\right] \quad (16)$$

$$g_0^{eq} = \sigma T - \bar{\omega}T$$

$$g_{1-6}^{eq} = \frac{1}{6}\bar{\omega}T\left(1 + \frac{\mathbf{e}_i\cdot\mathbf{u}}{c_{sT}^2}\right) \quad (17)$$

Two different lattice speeds of sound are used for the density and energy distribution functions to take advantage of the LMNA for numerical stability. The former is $c_s = \sqrt{1/3}$, and the latter is $c_{sT} = \sqrt{\bar{\omega}/3}$. $\bar{\omega}$ is maintained as 0.5 in this study. The heat capacity ratio, σ, is defined as $\frac{(\rho c)_{solid}}{(\rho c_p)_{gas}}$ for solid and $\frac{(\rho c_p)_{gas}}{(\rho c_p)_{gas}} = 1$ for the gas phase. σ is held as 1 for the species concentration equations. Like the combustion simulation using the LB method,[40,41,53] the density, temperature, and species are inherently interrelated. The macroscopic variables are derived as

$$\rho = \sum_i f_i,\ \rho\mathbf{u} = \sum_i f_i\mathbf{e}_i + \frac{\delta_t}{2}\rho\mathbf{F},\ \sigma T = \sum_i g_i,\ Y = \sum_i h_i \quad (18)$$

The fluid pressure, P, is recovered as $P = \rho c_s^2/\epsilon$. The macroscopic fluid velocity, $\mathbf{u}$, is involved in the source term, $\mathbf{F}$, as shown in eq 3. This quadratic equation of variable, $\mathbf{u}$, can be explicitly solved by introducing temporal velocity $\mathbf{v}$.[47]

$$\mathbf{u} = \frac{\mathbf{v}}{l_0 + \sqrt{l_0^2 + l_1|\mathbf{v}|}} \quad (19)$$

Here $\mathbf{v}$, l_0, and l_1 are as follows.

https://doi.org/10.1021/acs.energyfuels.2c03892
Energy Fuels 2023, 37, 5926−5941

$$\mathbf{v} = \frac{1}{\rho}\sum_i \mathbf{e}_i f_i - \varepsilon \mathbf{a},\ l_0 = \frac{1}{2}\left(1 + \varepsilon\frac{\delta_t \nu}{2\mathrm{K}}\right),\ l_1 = \varepsilon\frac{\delta_t F_\in}{2\sqrt{\mathrm{K}}} \tag{20}$$

The set of transport equations in eq 1 is recovered by the Chapman−Enskog analysis of the LB-MRT flow and thermal model.[38,54] The diagonal relaxation matrix $\mathbf{S}_{f,g,h}$ has a direct relationship with the effective kinematic viscosity, effective thermal diffusivity, and diffusion coefficient of species (tar and syngas)

$$\begin{aligned}\nu_e &= c_s^2\left(\frac{1}{\tau_\nu} - \frac{1}{2}\right)\delta_t,\ \alpha_e \\ &= c_s^2\left(\frac{1}{\tau_\alpha} - \frac{1}{2}\right)\delta_t,\ D \\ &= c_s^2\left(\frac{1}{\tau_D} - \frac{1}{2}\right)\delta_t\end{aligned} \tag{21}$$

where $\tau_{\nu,\alpha,D}$ are the relaxation rates to the fluid transport properties. The overall relaxation rates are given as

$$\begin{aligned}\mathbf{S}_f &= \mathrm{diag}(1,\ 1.1,\ 1.1,\ 1,\ 1.1,\ 1,\ 1.1,\ 1,\ 1.1,\ \tau_\nu,\ 1.1 \\ &\quad ,\ \tau_\nu,\ 1.1,\ \tau_\nu,\ \tau_\nu,\ \tau_\nu,\ 1.2,\ 1.2,\ 1.2) \\ \mathbf{S}_g &= \mathrm{diag}(1,\ \tau_{\alpha x},\ \tau_{\alpha y},\ \tau_{\alpha z},\ 1.2,\ 1.2,\ 1.2)\end{aligned} \tag{22}$$

Note that different relaxation rates can be chosen for the anisotropic thermal diffusivity. The bulk viscosity is assumed to be the same as the shear viscosity.

The numerical setup for the boundary is described in Figure 3. The general on-site velocity boundary condition[55] is chosen for the flow boundary condition with the fully developed flow velocity inlet and pressure outlet. This boundary treatment is a branch of the nonequilibrium bounce-back method, which satisfies the same order of accuracy as the flow domain. A constant wall temperature boundary condition is imposed for the thermal distribution function to emulate the reactor condition. Lastly, the species boundary condition is the zero-flux boundary condition, which is the condition for the reactor wall.

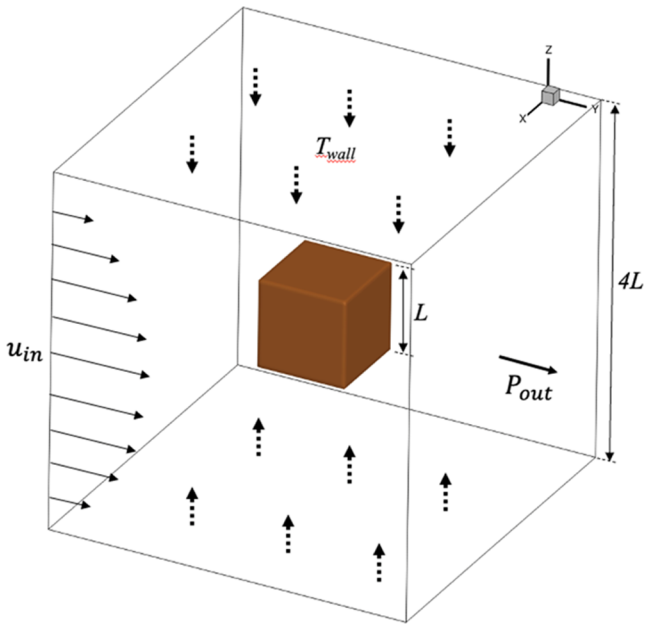

Figure 3. Numerical setup with the particle positioned at the center of domain.

2.3. Biomass Shrinkage Model. Biomass shrinkage is a sub-grid level phenomenon that needs to be considered without disturbing the governing equations. Proper modeling is required to avoid excessive computer time when simulating particle shrinkage. Here, the concept of the partially saturated cell[56] method is used to track the shrinking boundary of the solid. The method is further adapted to resolve both the fluid and solid lattices, considering the REV scale fluid flow and the heat transfer. First, the volume fraction is calculated at each timestep. Figure 4 shows an effective way to calculate the volume fraction of the interface lattice. For ease of interpretation, the 2D illustration is provided. The fluid and solid lattices are divided by the shrinking interface. The solid volume fraction of the interface lattices is calculated as a multilevel cell division. The six-level of cell division is shown in Figure 4.

The volume fraction, ϕ, is defined as the amount of porous solid volume out of the lattice cell volume.

$$\phi = \frac{V_{\text{solid frac}}}{V_{\text{lattice}}} \tag{23}$$

This volume fraction is used for calculating actual drag forces (eq 3) and the effective thermal conductivity of the partially saturated cell. It should be mentioned that thermal conductivity is a rate coefficient, so the harmonic mean is the correct way to represent the interface conductivity.[57]

$$F_{\mathrm{PSL}} = \phi F \tag{24}$$

$$\kappa_{\mathrm{PSL}} = \left(\frac{1-\phi}{\kappa_{\mathrm{gas}}} + \frac{\phi}{\kappa_e}\right)^{-1} \tag{25}$$

The subscript PSL refers to the partially saturated lattices where the interface intersects.

As discussed in the Introduction section, conversion is not the sole factor for biomass shrinkage. To incorporate the temperature effect, the experimental investigation by Davidsson and Pettersson[20] is used. Using birch wood (hardwood type), they formulated the time dependence of shrinkage, which can be implemented in the numerical model as

$$s = c^2(aT^2 + bT + c) \tag{26}$$

where s and c refer to the shrinkage and conversion defined as (1 − size/initial size) and (1 − mass/initial mass), respectively, and a, b, and c are the shrinkage coefficients that vary for different dimensions (i.e., longitudinal, tangential, and radial direction of biomass). The isotropic assumption is used, and the averaged value of all three directions is employed in the simulation. The valid temperature range for the current model is 623−973 K. Figure 5 shows the averaged dynamic shrinkage with respect to conversion in this temperature range with an increment of 50 K.

This shrinkage model is incorporated into the LB model and is executed at the beginning of every iteration to calculate the volume fraction-based properties. If the solid fraction becomes 0, the solid lattice is converted to the gas lattice. During the particle shrinkage, the densities of solids (i.e., biomass, intermediate solid, and char) must be conserved to accurately characterize the dynamic porosity and the final char density. The amount of solid quantity taken by volume shrinkage in each

https://doi.org/10.1021/acs.energyfuels.2c03892
Energy Fuels 2023, 37, 5926−5941

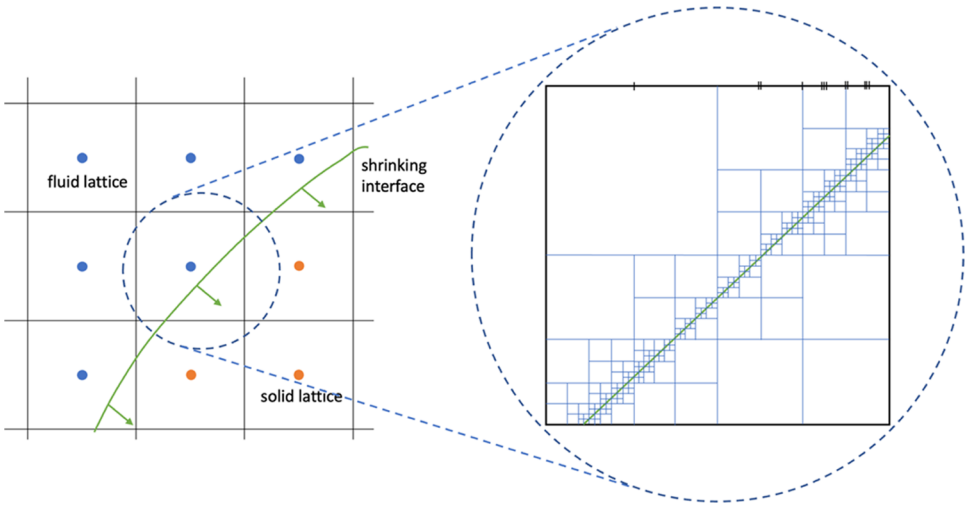

Figure 4. 2D illustration of biomass shrinkage modeling. The fluid and solid lattices are divided by the shrinking interface on the left-hand side. The center fluid lattice has a fraction of the solid lattice. This fraction is calculated by the recursive algorithm, visually shown on the right-hand side.

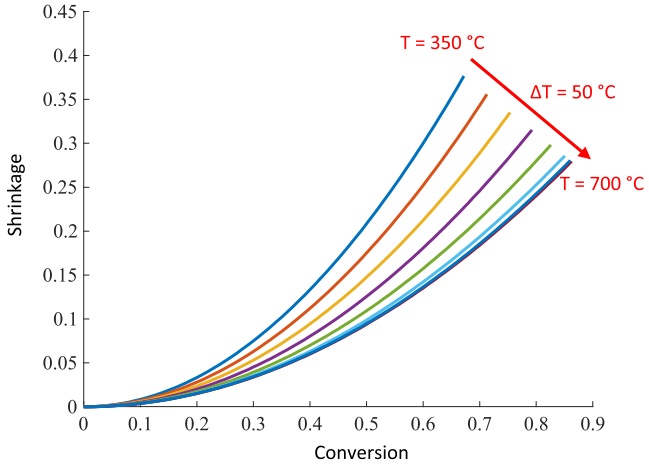

Figure 5. Dynamic shrinkage as a function of conversion.

lattice is summed up and redistributed to the particle. The current computer code is written in C++ and is parallelized using the hybrid message-passing interface (MPI) and OpenMP.

3. RESULTS AND DISCUSSION

This section describes the application of the present 3D LB and shrinkage models to simulate biomass particle pyrolysis, including experimental validations and parametric studies. All of the numerical simulations are performed using dimensionless parameters. The radiative heat transfer is neglected as the effect is negligible in the reactor condition compared with the convective heat transfer. The temperature-dependent properties, such as viscosity, thermal conductivity, and mass diffusion coefficient, are used for the gas phase, as shown in Table 2.[58] The physical properties of biomass are shown in Table 3. The effective biomass conductivity is described in eq 2. Sufficiently small grid size, dx, and the timestep, dt, are used to resolve the physicochemical details in each simulation case. The resultant relaxation parameter is in the range of 0.6−1.4, so the relaxation parameter is not too close to 0.5 for numerical stability and is not well over 1.0 for accuracy.

3.1. Validation.

Three different experimental cases using lab-scale single particles are used for model validation. Histories of the mass loss, shrinkage, and surface and center temperatures are validated. The particle is discretized to have enough resolution to resolve the interior of the porous particle. It is crucial to have a large enough gas domain because the thermal boundary layer caused by the conjugated condition plays an important role in predicting pyrolytic evolution. Figure 6 shows the cross-sectional temperature (left) and density (right) contours after 1.0 s, as an example. In this case, 5 mm cubic biomass is submerged in the reactor at a temperature of 873 K. At the initial stage of pyrolysis, a high-temperature gradient is formed by the conjugated condition between the gas and solid phases due to the large difference in thermal capacity.

The computational domain includes the biomass particle and surrounding gas with enough gas thickness to accurately account for the thermal boundary layer. The effect of the size of the gas domain was studied, as shown in Figure 7. For the 5 mm particle, the temperature error is negligible once the gas domain thickness is over 7.5 mm. The temperature error is defined as the deviation from the true value of the particle surface temperature after 10,000 timesteps. The true value is assumed as the highest domain surface temperature, where the domain thickness is 17.5 mm. As a result, the gas domain thickness over 7.5 mm is considered enough for the thermal boundary layer to develop fully near the particle surface. The gas domain size is set

Table 2. Physical Properties of Argon Gas for Temperature Range of 300−1000 K

temperature, T (K)	thermal diffusivity, α ($m^2\ s^{-1}$)	kinematic viscosity, ν ($m^2\ s^{-1}$)	heat capacity, C_p ($m^2\ s^{-2}\ K^{-1}$)
300	2.09×10^{-5}	1.41×10^{-5}	521
500	5.24×10^{-5}	3.80×10^{-5}	520
638	7.97×10^{-5}	5.26×10^{-5}	520
783	11.17×10^{-5}	7.32×10^{-5}	520
973	16.36×10^{-5}	10.79×10^{-5}	520

https://doi.org/10.1021/acs.energyfuels.2c03892
Energy Fuels 2023, 37, 5926−5941

Table 3. Thermal Properties of Biomass[8,29]

property	value
specific heat capacity of biomass, c_b	$1500 + 1.0T$ (J kg^{-1} K^{-1})
specific heat capacity of char, c_c	$420 + 2.09T + 6.85 \times 10^{-4}\ T^2$ (J kg^{-1} K^{-1})
specific heat capacity of tar, $c_{p,t}$	$-100 + 4.4T - 1.57 \times 10^{-3}\ T^2$ (J kg^{-1} K^{-1})
specific heat capacity of syngas, $c_{p,syn}$	$770 + 0.629T - 1.91 \times 10^{-4}\ T^2$ (J kg^{-1} K^{-1})
thermal conductivity of wood (in x, y, and z directions), κ_w	0.1046, 0.255, 0.255 (W m^{-1} K^{-1})
thermal conductivity of char (in x, y, and z directions), κ_c	0.071, 0.105, 0.105 (W m^{-1} K^{-1})
pore diameter, d	$5 \times 10^{-5}\ (1 - \eta) + 1 \times 10^{-4}\ \eta$ (m)

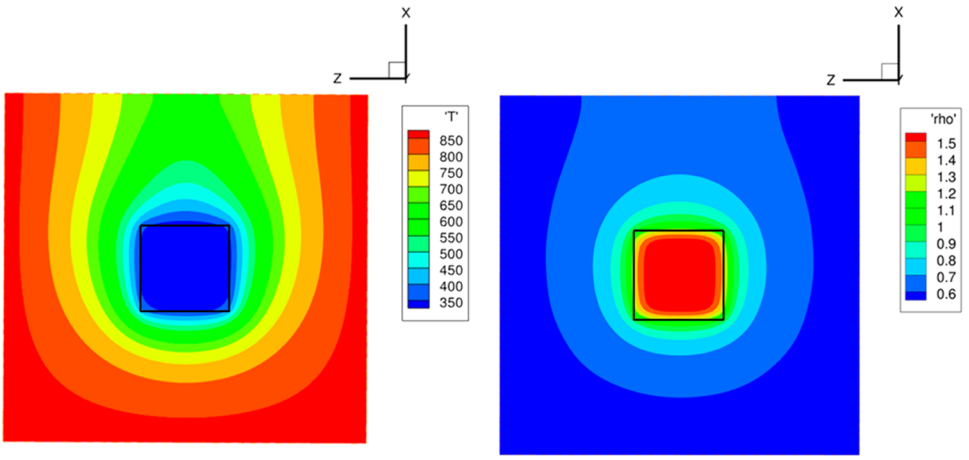

Figure 6. Temperature (left, in Kelvin) and density (right, kg m^{-3}) contours after 1.0 s (5 mm cube biomass submerged in the reactor at a temperature of 873 K). The black square represents the interface between gas and solid.

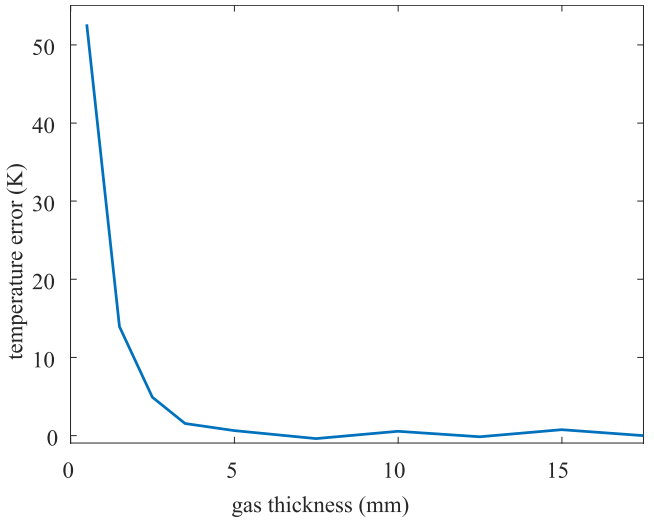

Figure 7. Calculated temperature error for the 5 mm particle after 10,000 timesteps as a function of the gas domain thickness.

to be four times the characteristic particle length for all three validation cases, as shown in Figure 3.

To accurately validate experimental cases, the reactor temperature and the inlet velocity play an important role. Based on the inlet velocity, the magnitude of the forced convection heat transfer is determined. The Richardson number (Ri) is a good indicator defined as the natural convection relative to the forced convection.

$$Ri = \frac{g\beta(T_\infty - T_s)D}{u^2} \tag{27}$$

Here g is the gravity, β is the thermal expansion coefficient, T_∞ is the reactor temperature, T_s is the solid particle temperature, D is the characteristic length of the solid particle, and u is the inlet velocity. For all three experimental cases, the resultant Ri number range is $1 < Ri < 5$, so both the free and forced convection have to be considered. It clearly shows that using the predefined convection coefficient based on either natural or forced convection in the literature will introduce numerical errors. In addition, the biomass product outflux will alter the overall heat transfer. In the current modeling approach, taking advantage of the conjugate heat transfer model, both heat transfer aspects are considered through eqs 3 and 11.

3.1.1. Case 1. Davidsson and Petterson (2002). Davidsson and Petterson[20] investigated the pyrolysis of 5 mm cube birch wood (hardwood type). Three different temperatures were studied for validation (773, 873, and 983 K). As with the experimental setup, preheated argon gas with the same inlet velocity of 0.01 m s^{-1} was used in the simulation. The dried room-temperature cubicle particle with an average density of 600 kg m^{-3} was submerged into the preheated domain abruptly to initiate the pyrolysis process. The grid size, dx, and timestep, dt, were set as 2×10^{-4} m, and 1×10^{-4} s, respectively. Figure 8 shows the particle mass over time at different reactor temperatures. The particle mass is normalized by the initial mass. Good levels of agreement were obtained in particle mass loss.

3.1.2. Case 2. Park et al. (2010). Park et al.[8] experimentally investigated the pyrolysis of a one-inch spherical maple wood particle (hardwood type). Six temperatures ranging from 638 to 879 K were simulated for the present validation. Preheated argon gas with the same inlet velocity of 0.1 m s^{-1} as the experimental setup was used in the simulation. The room-temperature-dried particle with an average density of 630 kg m^{-3}

https://doi.org/10.1021/acs.energyfuels.2c03892
Energy Fuels 2023, 37, 5926−5941

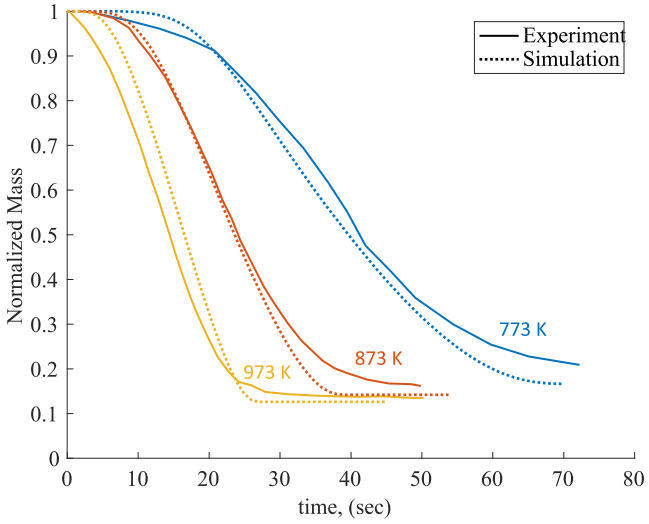

Figure 8. Normalized mass for different reactor temperatures.

was submerged into the preheated domain abruptly to initiate the pyrolysis process. The grid size, dx, and timestep, dt, were set as 5×10^{-4} m, and 5×10^{-4} s. Figure 9 shows the evolution of the

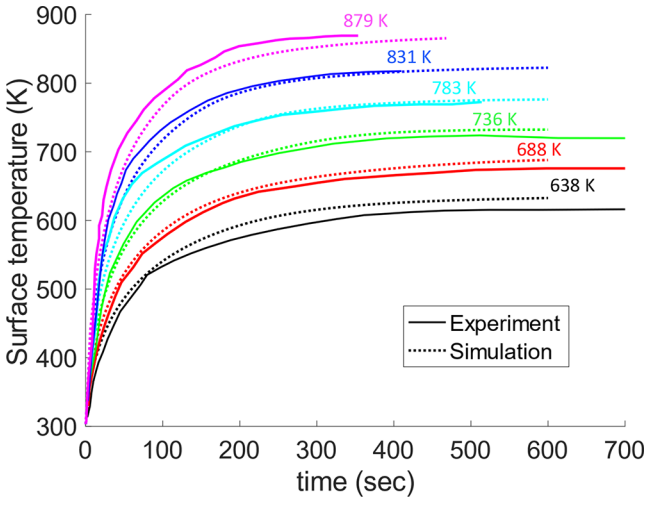

Figure 9. Biomass particle surface temperature evolutions at different reactor temperatures.

biomass surface temperature at different reactor temperatures. The simulated results (dotted line) closely follow the experimental data (solid line) for the conditions studied.

This modeling study considers conjugate heat transfer at the solid–gas interface. It should be noted that many modeling studies assume constant temperature or heat flux at the interface. Such assumptions are believed to introduce errors. For most biomass pyrolysis modeling, the convection coefficient is calibrated using experimental data, which can cause difficulties in validating the surface temperature without considering conjugate heat transfer. Furthermore, the advection of the pyrolysis product's off-gassing out of the biomass particle plays a significant role in the overall heat transfer and must be incorporated, as shown in eq 5. Thus, it is believed that the modeling of conjugate heat transfer at the interface is properly handled in this study.

The predicted center temperatures are also compared with the experimental data, as shown in Figure 10. The center

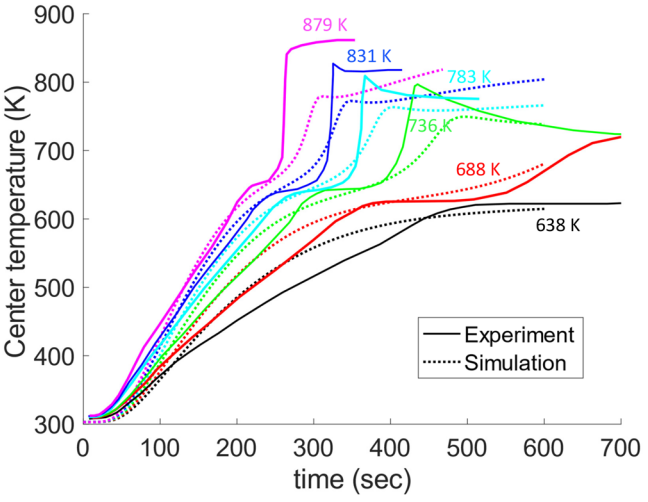

Figure 10. Biomass particle center temperature evolutions at different reactor temperatures.

temperature increases linearly at the initial stage due to heating. After that, the rate of increase decreases because of the endothermic reactions during the initial thermal decomposition of biomass. The exothermic reactions follow, resulting in a dramatic temperature increase. This increase is due to the secondary reaction of tar decomposition and the exothermic decomposition of the intermediate solid, as shown in Figure 1. The present simulation predicts a faster heat outflux than the experiment. Therefore, the predicted peak center temperature is not as high as the experimental data.

The predicted solid mass fraction is compared with experimental data, as shown in Figure 11. Good levels of agreement are obtained in all temperature ranges.

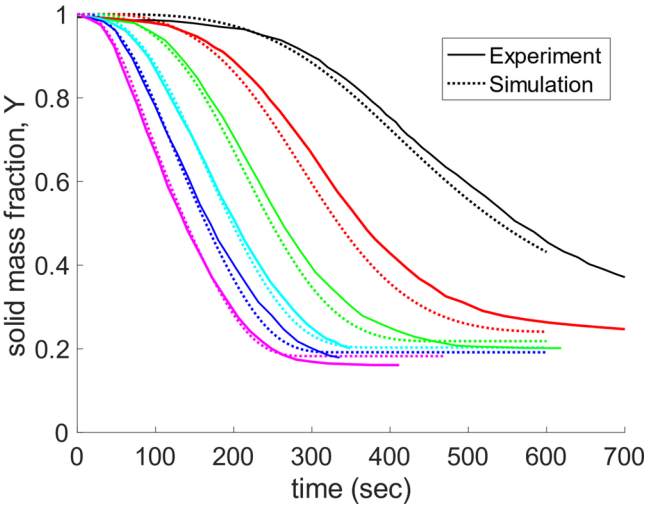

Figure 11. Normalized biomass particle mass evolutions at different reactor temperatures.

3.1.3. Case 3. Caposciutti et al. (2019). Caposciutti et al.[9] investigated the pyrolysis of spherical beech wood (hardwood type) of two different sizes (small: 15 mm, big: 25 mm). The reactor temperature was increased slowly at around 25 K min^{-1} to measure the biomass shrinkage. The room-temperature-dried particle with an average density of 705 kg m^{-3} was used in the present simulation, which is the same as in the experimental

https://doi.org/10.1021/acs.energyfuels.2c03892
Energy Fuels 2023, 37, 5926–5941

setup. The particle was submerged into the gas domain with the grid size $dx = 5 \times 10^{-4}$ m and timestep $dt = 1 \times 10^{-3}$ s. Figures 12

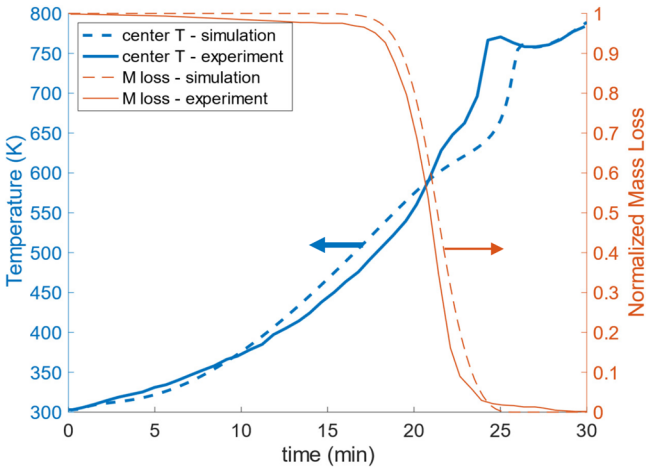

Figure 12. Particle center temperature and normalized mass loss for the 25 mm particle.

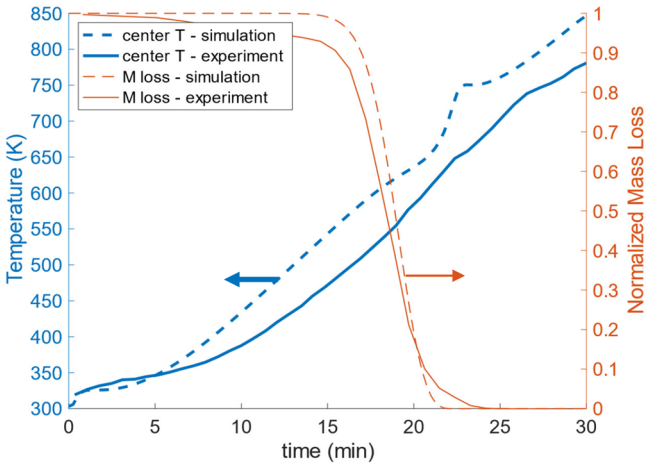

Figure 13. Particle center temperature and normalized mass loss for the 15 mm particle.

and 13 show the particle center temperature and the normalized mass loss of the big and small particles, respectively. The normalized mass loss is formulated as $M_{loss} = \frac{M_o - M}{M_o - M_f}$, where M_o, M_f, and M are initial, final, and current mass, respectively. The predicted results follow the experimental data closely for the 25 mm particle. The predicted center temperature of the 15 mm particle rises faster than the experimental data, but the mass loss is reasonably predicted.

The predicted volume shrinkage is also compared with the experimental data, as shown in Figure 14. The shrinking timing is predicted reasonably well. The final volume shrinkage for the 25 mm particle is around 0.48 and for the 15 mm particle is about 0.39. It is worth noting that the predicted final shrinkage ratio of the 15 mm particle was higher than that of the 25 mm particle, matching the experimental data. The biomass porosity contour evolution of the 25 mm particle is shown in Figure 15. Due to the shrinkage, the particle diameter is decreased by the power of one-third of the final volume, $\sqrt[3]{0.48} = 0.78$. Thus, the final biomass diameter is 78% of the initial biomass diameter. In addition, the final porosity of the particle is predicted to be $\varepsilon \approx 0.7$, which is consistent with the average char porosity in the literature. Without shrinkage modeling, there is a possibility of overpredicting the porosity, leading to inaccurate results by overestimating heat and momentum transfer. The current case was tested again without the shrinkage model, and the final porosity turned out to be $\varepsilon \approx 0.9$, which is an unrealistic char porosity.

3.2. Parametric Study. Fast pyrolysis involves multiscale physicochemical phenomena. These various scales of phenomena are interrelated and difficult to analyze experimentally. In this parametric study, the effects of particle scale and sub-particle scale are studied separately.

3.2.1. Particle Scale Effect. Predicting the product yield and conversion time is important to evaluate the performance of a biomass pyrolysis reactor. The particle size, gas inlet velocity, and reactor gas temperature are varied in the present simulation. Figure 16a shows the effect of biomass particle size on the product yield and conversion time. A spherical biomass particle is simulated, and its diameter varies from 1 to 50 mm. The temperature and gas velocity are fixed as 831 K and 0.1 m s^{-1}, respectively. It is seen that the conversion time increases quadratically with the increase in particle size. The dimensionless Fourier number ($Fo = \alpha t/L^2$) is shown on the same plot to identify the effect of the particle size. Here, α is the diffusion coefficient of wood ($\alpha = (\kappa/\rho c)_{biomass}$); t is the conversion time; and L is the diameter of the spherical biomass particle. Based on the conversion time, the Fourier number can be viewed as the ratio of the heat transfer rate to the heat-storing rate up to the moment. It is shown that the Fourier number decreases with the increased particle size, meaning the overall heat transfer is hindered as the particle size increases. It is a clear example that the effect of particle sizes can be attributed to internal heat transfer.

The particle size also affects the final product yields, as shown in Figure 16b. A large particle will produce higher char production but lower tar and syngas. This trend can be explained by the following. As the size increases, it is harder for the produced tar to go out of the biomass particle, leading to secondary tar breakdown to char.

To investigate the effect of the inlet gas velocity, a 5 mm cube biomass particle is submerged in the reactor at 973 K. The inlet velocity is varied from 0.02 to 0.8 m s^{-1} to simulate the conditions under a laminar flow regime. As shown in Figure 17, the increased flow velocity around the biomass particle reduces the conversion time. However, the change in the final product yield is minimal. The faster conversion time can be explained by the thinner thermal boundary layer. Figure 18 shows the temperature contour of a 5 mm cube biomass particle after 2 s of biomass submersion. As the gas velocity is doubled from 0.1 to 0.2 m s^{-1}, the thermal boundary layer thickness is decreased by 24% (from 5.88 to 4.47 mm) due to the increased advection of the gas phase. Eventually, this decreased thickness accelerates biomass conversion by increasing the overall heat flux.

The reactor temperature is a critical parameter in pyrolysis and greatly affects the pyrolytic reaction. The simulation conditions are based on those of validation case 2 (Park et al.[8]). The conversion rate increases with the increased reactor temperature, as shown in Figure 19. The corresponding Péclet number (Pe) is shown in the same plot to analyze the temperature effect. The thermal Péclet number is the product of the Reynolds number and the Prandtl number and is defined

https://doi.org/10.1021/acs.energyfuels.2c03892
Energy Fuels 2023, 37, 5926−5941

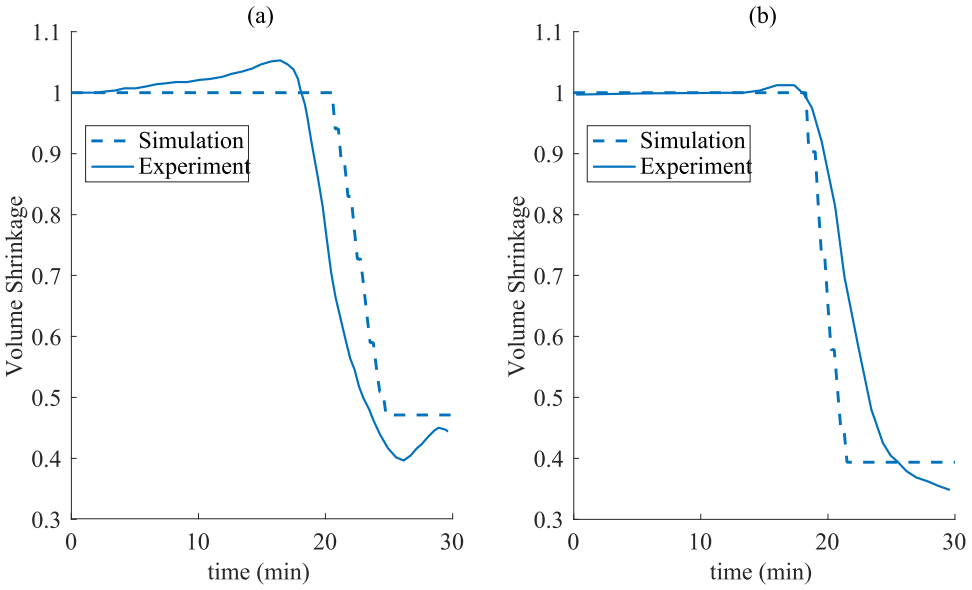

Figure 14. Volume shrinkage history of (a) 25 mm (b) 15 mm particles.

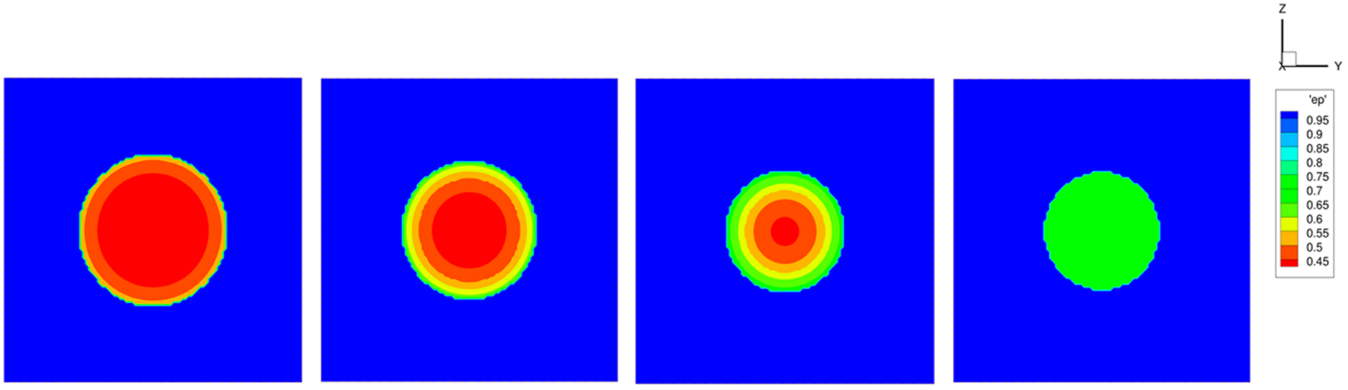

Figure 15. Porosity contour at the center cross section of 25 mm particle at different times (from left: 20, 22, 24, and 26 min).

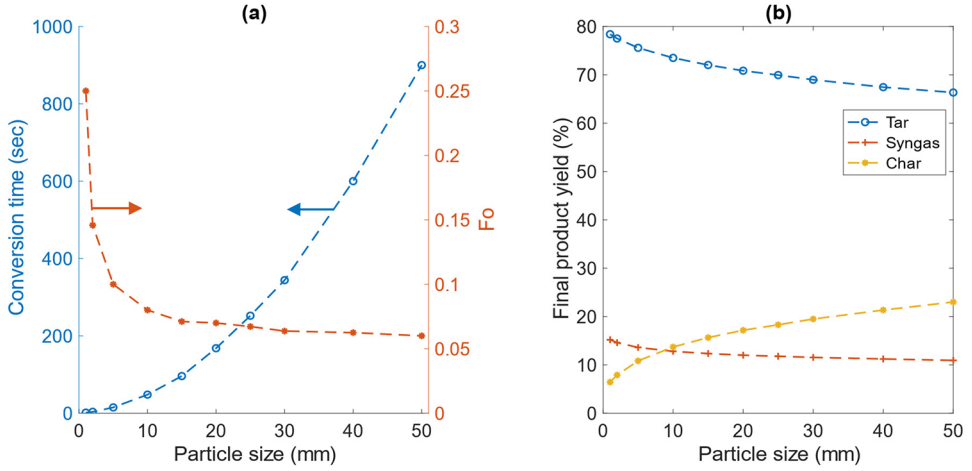

Figure 16. Effect of biomass particle size on (a) conversion time and Fourier number and (b) final product yield.

as $Pe = Re\ Pr = Lu/\alpha$, where u and α are the gas velocity and the thermal diffusion coefficient of the gas, respectively. Here, the maximum velocity at the particle middle point (the point between the particle center and the surface) is considered. The Péclet number is the ratio of the advective transport rate to the diffusive transport rate. It is shown that the internal advective heat transfer becomes more dominant and cannot be ignored as the reactor temperature increases. The tar yield approaches its maximum as the reactor temperature increases, and so does syngas production. The char yield is reduced with increasing temperature. It can be explained that the higher thermal energy

https://doi.org/10.1021/acs.energyfuels.2c03892
Energy Fuels 2023, 37, 5926−5941

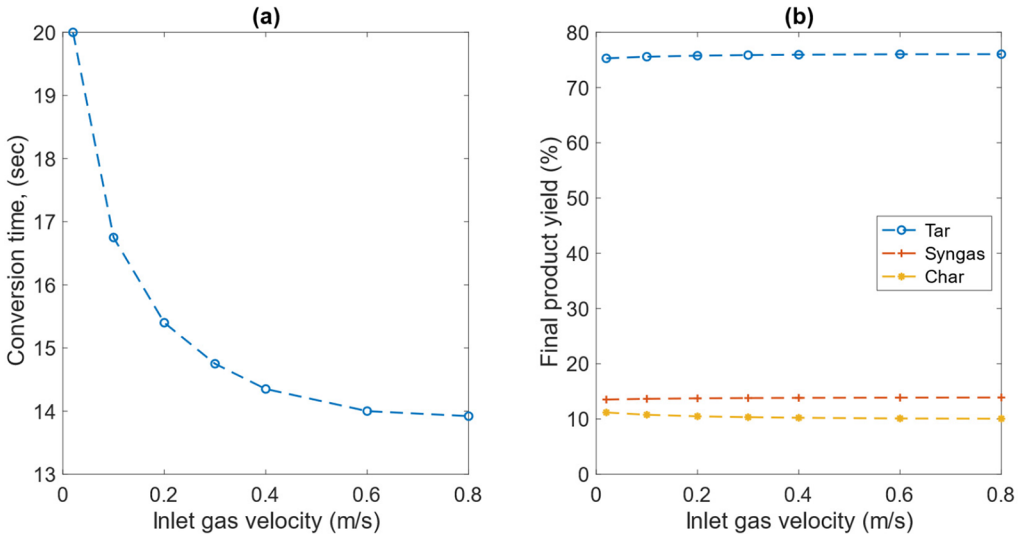

Figure 17. Effect of inlet velocity on (a) conversion time and (b) final product yield.

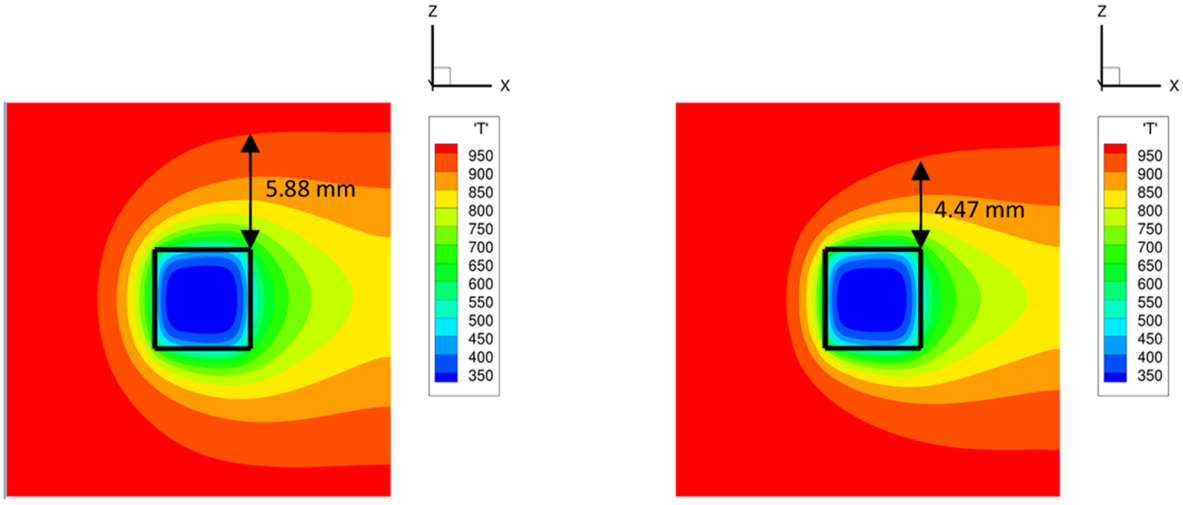

Figure 18. Thermal boundary layer thickness for inlet gas velocity of 0.1 m s^{-1} (left) and 0.2 m s^{-1} (right) after simulation time of 2 s.

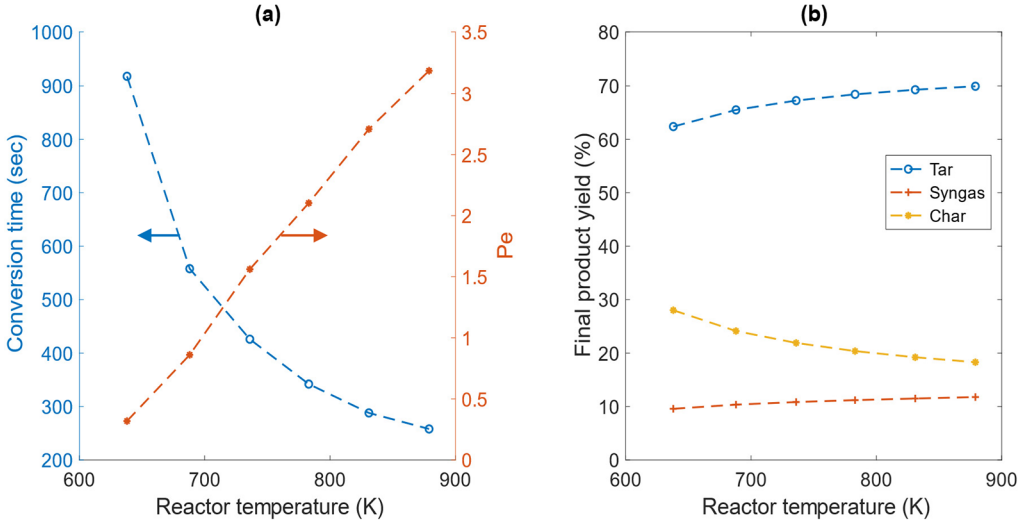

Figure 19. Effect of reactor temperature on (a) conversion time and Péclet number and (b) final product yield.

induces more thermal decomposition into the lighter hydrocarbons.

3.2.2. Sub-Particle Scale Effect. Modeling the sub-particle scale phenomena is necessary as the porosity and permeability of

https://doi.org/10.1021/acs.energyfuels.2c03892
Energy Fuels 2023, 37, 5926−5941

biomass change over time, causing the gaseous products to diffuse out of the biomass particle differently. The overall heat transfer is affected by the above evolving sub-particle properties and phenomena. Simulations with various deactivated sub-models were conducted for the 5 mm cube particle at the reactor temperature of 873 K (case 1). Figure 20 shows that if the gas

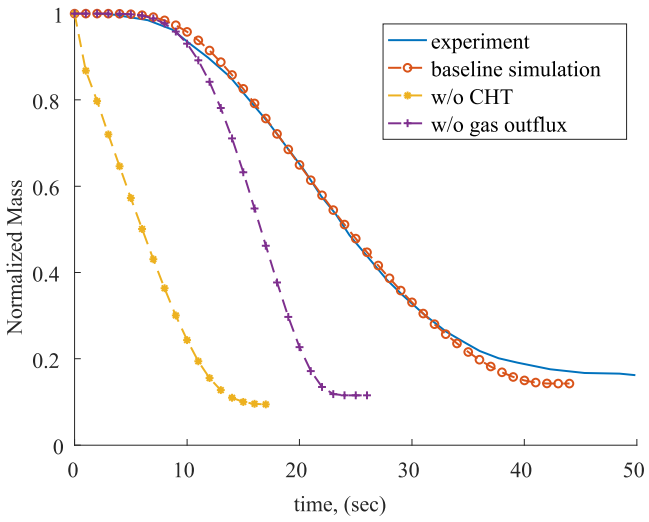

Figure 20. Effect of sub-particle scale modeling.

outflux is not considered (i.e., the internal advection of gaseous products is removed), the particle conversion time is halved. The initial conversion is accurately captured, but a steeper mass loss is detected as the particle evolves. Note that when the gas outflux is considered (i.e., baseline case), the efflux of gaseous products hinders the advective heat transfer going into the particle. Conversely, not considering the gas outflux will cause a higher advective heat transfer, resulting in a shorter conversion time.

On the effect of conjugate heat transfer modeling, the thermal boundary layer is not formed around the particle if the conjugated condition is not posed at the solid−gas interface. Thus, the high-temperature gas directly heats the particle, leading to an unrealistically fast conversion. It is concluded that considering both the thermal boundary layer induced by the conjugated interface condition and the gaseous product efflux from the porous biomass particle is important in modeling the pyrolysis process.

The biomass porosity and permeability vary over time in the current modeling approach; these parameters are evaluated based on the local solid composition to emulate the realistic particle evolution. On the one hand, porosity is the number of passages in each local cell of interest, defined as the ratio of gas volume fraction to solid volume fraction. On the other hand, permeability is how wavy the passage is. The permeability is calculated based on the pore diameter and porosity of the specific location of interest, as shown in eq 4. The permeability can vary from 10^{-12} to 10^{-6} m^2 based on the composition of the solid during the conversion.[59] The permeability remains constant for the purpose of the present parametric study. The conversion time is shown in Figure 21. To characterize the effect of permeability, the conditions of Case 2 were used with a reactor temperature of 773 K.

The result in Figure 21 is divided into three regimes. In the low-permeability region (10^{-12} to 10^{-10} m^2), the gas velocity in the pore is low and heat is mainly transferred by conduction

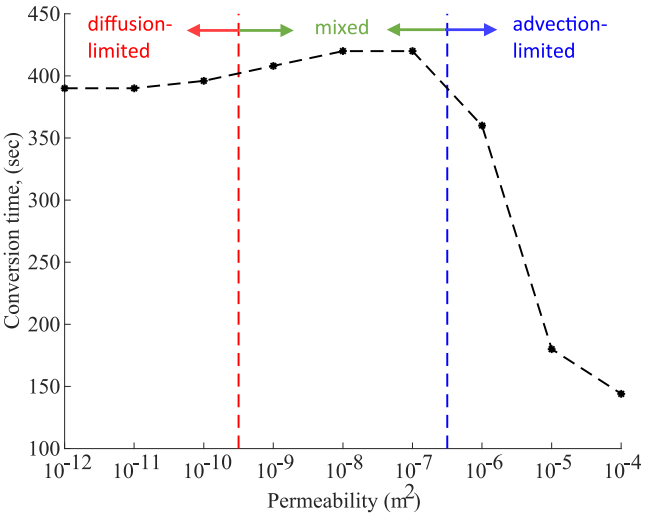

Figure 21. Effect of particle permeability on conversion time.

(diffusion-limited). As the permeability increases (10^{-9} to 10^{-7} m^2), the gaseous product efflux increases, hindering inward heat transfer and overall conversion. At high permeability (10^{-6} to 10^{-4} m^2), the gas advection inside the porous biomass becomes dominant, causing a high heat transfer rate and conversion. In this regime, the gaseous product's volume fraction is relatively low and does not block the advective flow outside the particle. Note that the permeability of pure woody biomass is around 10^{-12} m^2 initially, and the particle will experience different permeability regimes when evolving. Care must be taken in predicting permeability because an increase in permeability can increase or decrease the overall conversion time.

Crowley et al.[60] calculated the permeability of biomass and biochar, in which the actual biochar geometry was reconstructed using X-ray computed tomography. Permeabilities were calculated based on Darcy's law by solving the reconstructed geometry numerically. In the paper by Crowley et al., the predicted permeability of biochar is in the range of 10^{-12} m^2, which is lower than the measurement ($\sim 10^{-6}$ m^2) by Wałowski.[59] Multiple methods of calculating permeability are available, and the resultant values vary significantly. The geometric irregularity of biochar also makes it difficult to generalize the permeability value.

3.3. Heat Transfer Coefficient. As shown in Figure 20, modeling of the gas outflux plays a significant role in predicting the conversion time. Simulations that did not consider the product gas outflux predicted nearly half of the overall conversion time. Typically, the "one-way coupling" approach was used in determining the heat transfer coefficient, i.e., either the conventional heat transfer models[61,62] were used or the experimental convection heat transfer coefficients were empirically formulated. But this study considers conjugate heat transfer, a two-way coupling approach. Based on the current simulation, the Nusselt number under the pyrolysis condition is analyzed. The Nusselt number can be directly calculated as the ratio of the surface heat flux and the temperature difference between the gas and solid phase by resolving the thermal boundary layer. The averaged Nusselt number is represented as an integral surface form

$$Nu = \frac{1}{S}\iint_S (Nu_{\text{local}}\cdot\vec{\mathbf{n}})\mathrm{d}S \tag{28}$$

https://doi.org/10.1021/acs.energyfuels.2c03892
Energy Fuels 2023, 37, 5926−5941

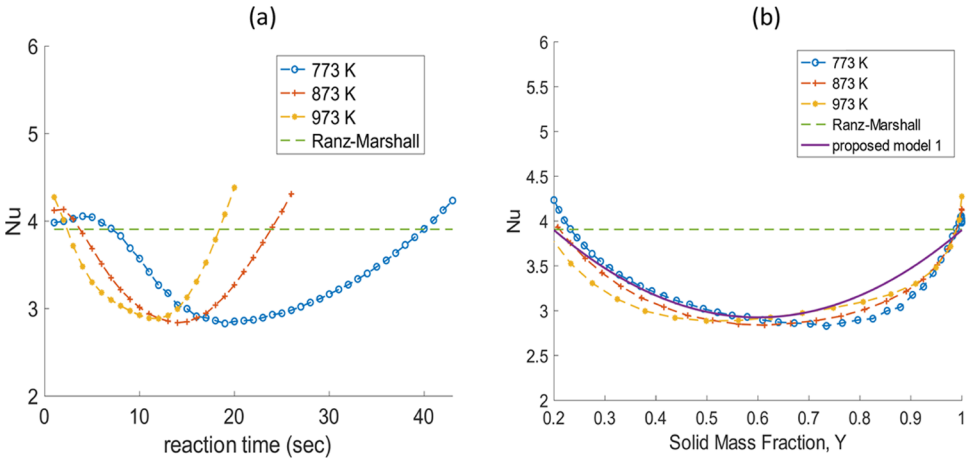

Figure 22. Nusselt numbers at different reactor temperatures as a function of (a) reaction time (s) and (b) dimensionless solid mass fraction.

where $\vec{\mathbf{n}}$ is the surface normal vector and S is the surface area of the particle. The local Nusselt number is defined as $Nu_{\text{local}} = \frac{\partial(T_s - T_g)/\partial x}{(T_s - T_\infty)/L}$, where T_s and T_g refer to the gas and solid temperatures, respectively, adjacent to each other with the discrete length (∂x), T_∞ is the reactor temperature, and L is the characteristic length of the particle.

The predicted Nusselt numbers as a function of time and dimensionless mass fraction are compared at different reactor temperatures, as shown in Figure 22. For the test cases, a spherical particle of 100 mm^3 in volume was submerged in the inflow of 0.2 m s^{-1}. Compared to the Ranz and Marshall model $(Nu = 2.0 + 0.6\sqrt{Re}\,Pr^{1/3})$, the predicted Nusselt number changes with time. Although the predicted Nusselt number starts with a similar value to that obtained from the Ranz and Marshall model, it decreases by 25% in all three temperatures. Based on the simulation results, a new correlation is formulated, as shown in eq 29. The proposed model 1 is a function of the solid mass fraction of the particle and the conventional Nusselt number obtained from the Ranz and Marshall model.

$$Nu_{\text{proposed}} = \begin{cases} (1.563Y^2 - 1.875Y + 1.313)Nu, & Y \geq 0.2 \\ Nu, & Y < 0.2 \end{cases} \tag{29}$$

$$h_{\text{proposed}} = h_0 - 359.3_m \tag{30}$$

Another correlation is proposed, which is a linear regression model shown in eq 30. Figure 23 shows the predicted convection heat transfer coefficients as a function of mass flux out of the particle at different reactor temperatures. The result obtained using eq 30 is also shown in Figure 23 as "proposed model 2." The intercept h_0 can be evaluated from the conventional Nusselt number correlation, such as Ranz and Marshall's model, calculated as $h_0 = \frac{Nu \cdot k}{L}$, where k is the temperature-dependent thermal conductivity of the gas.

A sensitivity study was conducted to test two proposed models. The parameters are particle size, inlet velocity, and geometry. The L_2 relative error norm is used for the analysis and shown as

$$L_2 \text{ relative error} = \sqrt{\frac{\sum(\phi_{\text{data}} - \phi_{\text{model}})^2}{\sum(\phi_{\text{data}})^2}} \tag{31}$$

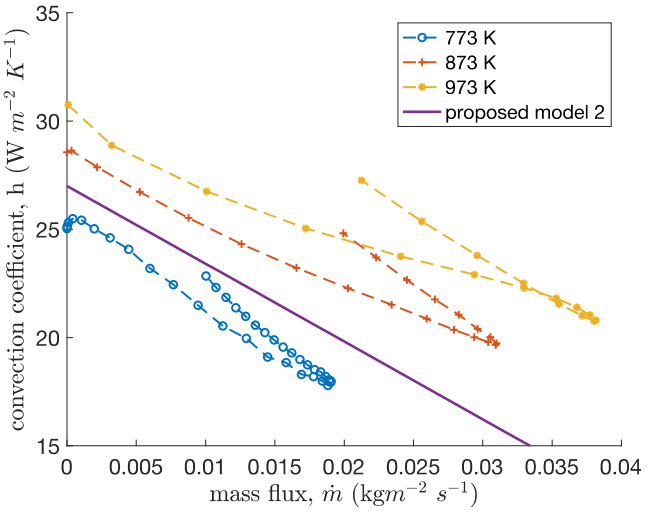

Figure 23. Convection heat transfer coefficients at different reactor temperatures as a function of mass flux.

where ϕ_{data} is from the current simulation and ϕ_{model} is the model prediction based on the same inputs as the simulated conditions. The baseline condition is set for all three sensitivity studies (Tables 4–6) as the 100 mm^3 spherical particle under the 0.2 m s^{-1} inflow and 873 K temperature. The sensitivity study focuses on the modeling accuracy under commonly studied pyrolysis conditions in the fluidized bed. Regardless of the different particle sizes and inlet velocities used, the proposed

Table 4. Sensitivity of Particle Size

L_2 relative error	2 mm	4 mm	8 mm
Ranz and Marshall[62]	0.3443	0.2813	0.1315
proposed model 1	0.1747	0.0986	0.0740
proposed model 2	0.1094	0.0901	0.0691

Table 5. Sensitivity of Inlet Velocity

L_2 relative error	0.4 m s^{-1}	0.6 m s^{-1}	0.8 m s^{-1}
Ranz and Marshall[62]	0.1783	0.1513	0.1773
proposed model 1	0.0386	0.0817	0.0797
proposed model 2	0.0836	0.0727	0.0901

https://doi.org/10.1021/acs.energyfuels.2c03892
Energy Fuels 2023, 37, 5926−5941

Table 6. Sensitivity of Different Geometries

L_2 relative error	sphere	cube	prolate spheroid
Richter and Nikrityuk[61]	0.1448	0.2278	0.3692
proposed model 1	0.0862	0.1223	0.1859
proposed model 2	0.0943	0.1158	0.1875

models show improved accuracy. It is noted that the error is independent of size and velocity.

The effect of biomass particle geometry was studied to take advantage of the present 3D simulations without using a predefined convection heat transfer coefficient. Three commonly studied geometries (sphere, cube, and prolate spheroid) shown in Figure 24 were tested. To achieve a fair comparison, three particles have the same volume of 100 mm^3. The characteristic length and surface area are important parameters for the conversion time. As the characteristic length decreases, conversion is accelerated. It is noted that the difference in the overall product yield is less than 1% for different geometries. The sensitivity study in Table 6 shows that the proposed models can reduce the predicted error by half. The Nusselt number from Richter and Nikrityuk's model[61] is used in the proposed model to incorporate different geometries.

The current investigation can be used to improve the heat transfer model for biomass reactor simulation. Both proposed models can be readily utilized for simulating biomass pyrolysis because of their simple hybrid formulations. Model 1 is based on the solid mass fraction, while Model 2 is based on the mass flux of the volatiles. These two quantities are complementary for a biomass particle. Each model has its unique advantages, and the user can choose a more suitable model for their application. Model 1 is more desirable if the surface geometry is difficult to determine. Additionally, the solid mass fraction can be easily calculated at every timestep without computational burdens. Model 2 is simple and tends to be more accurate, independent of the ash content and the remaining char during pyrolysis.

In summary, the LB method is suitable for solving complex geometries. The conjugate heat transfer between the gas and solid phase can be formulated readily, and no coupling is required. The LB method is an intrinsically transient simulation that is beneficial to biomass particle pyrolysis simulations. The simulation is generally more efficient than the typical finite volume-based simulation. The discrete element method can be implemented into the current LB framework for simulating fluidization in a biomass pyrolysis reactor.

4. CONCLUSIONS

Pyrolysis of biomass particles was simulated using the Lattice Boltzmann method that considers particle shrinkage, reaction kinetics, conjugate heat transfer, and gas flows inside the porous particle. The present numerical method was validated using three different experiments. Good levels of agreement were obtained in the shrinkage history, particle surface temperature, center temperature, mass loss, and conversion time. The predicted final char porosity was reasonable and similar to the literature data.

Parametric studies were conducted to investigate the sub-particle and particle scale effects. Results show that the internal heat transfer is affected by the particle size and reactor temperature. The Fourier number decreases to a nearly constant value as the particle size increases. The Péclet number increases linearly with the reactor temperature. Increasing the particle size has a negative effect on tar and syngas yields because it is harder for the gaseous products to leave the particle. A faster conversion is achieved with an increased inlet velocity by reducing the thermal boundary layer thickness. A high reactor temperature accelerates the secondary reaction, leading to an increase in lighter hydrocarbon products.

The conjugate heat transfer at the gas−solid interface needs to be considered in the simulation; a realistic permeability needs to be used for simulating the product gas outflux. Without considering these sub-particle effects, the predicted conversion will be too fast. It was found that permeability is an important parameter, and its effect can be divided into three regimes: diffusion-limited, mixed, and advection-limited. The gaseous product efflux delays the overall conversion in the mixed regime. Modified heat transfer coefficients are proposed and validated based on the present simulation results. The proposed models can potentially improve the heat transfer modeling accuracy in the reactor scale modeling.

AUTHOR INFORMATION

Corresponding Author

Song-Charng Kong − *Department of Mechanical Engineering, Texas Tech University, Lubbock, Texas 79409, United States;* orcid.org/0000-0002-8060-1396; Email: sokong@ttu.edu

Author

Yongsuk Cho − *Department of Mechanical Engineering, Iowa State University, Ames, Iowa 50011, United States*

Complete contact information is available at:

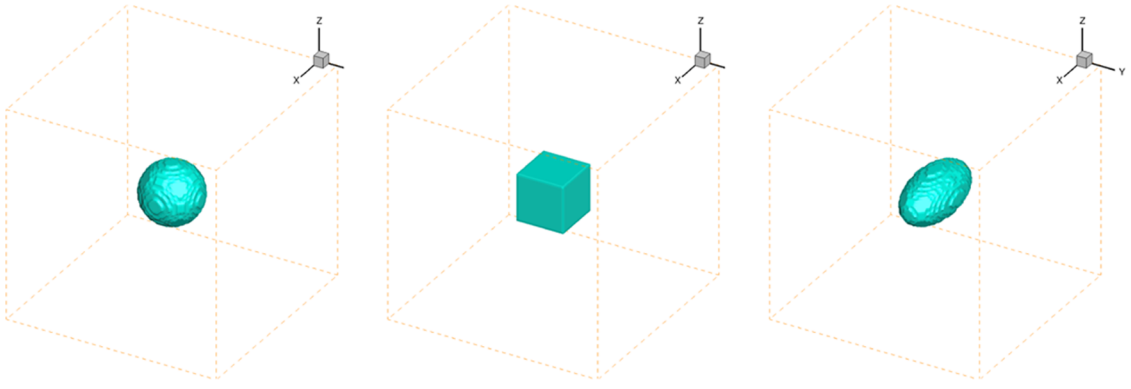

Figure 24. Different biomass particle geometries (sphere, cube, and prolate spheroid).

https://doi.org/10.1021/acs.energyfuels.2c03892
Energy Fuels 2023, 37, 5926−5941

https://pubs.acs.org/10.1021/acs.energyfuels.2c03892

Notes

The authors declare no competing financial interest.

■ ACKNOWLEDGMENTS

This research was supported by the National Science Foundation (CBET-2219665).

■ REFERENCES

(1) Mauser, W.; Klepper, G.; Zabel, F.; Delzeit, R.; Hank, T.; Putzenlechner, B.; Calzadilla, A. Global biomass production potentials exceed expected future demand without the need for cropland expansion. *Nat. Commun.* **2015**, *6*, No. 8946.

(2) Gielen, D.; Gorini, R.; Wagner, N.; Leme, R.; Gutierrez, L.; Prakash, G.; Asmelash, E.; Janeiro, L.; Gallina, G.; Vale, G. *Global Energy Transformation: A Roadmap to 2050*; International Renewable Energy Agency, 2019.

(3) Pecha, M. B.; Arbelaez, J. I. M.; Garcia-Perez, M.; Chejne, F.; Ciesielski, P. N. Progress in understanding the four dominant intra-particle phenomena of lignocellulose pyrolysis: chemical reactions, heat transfer, mass transfer, and phase change. *Green Chem.* **2019**, *21*, 2868−2898.

(4) Silva, R.; Romeiro, G.; Veloso, M.; Figueiredo, M.-K.; Pinto, P.; Ferreira, A.; Gonçalves, M.; Teixeira, A.; Damasceno, R. Fractions composition study of the pyrolysis oil obtained from sewage sludge treatment plant. *Bioresour. Technol.* **2012**, *103*, 459−465.

(5) Mohan, D.; Pittman, C. U., Jr; Steele, P. H. Pyrolysis of wood/biomass for bio-oil: a critical review. *Energy Fuels* **2006**, *20*, 848−889.

(6) Ciesielski, P. N.; Pecha, M. B.; Lattanzi, A. M.; Bharadwaj, V. S.; Crowley, M. F.; Bu, L.; Vermaas, J. V.; Steirer, K. X.; Crowley, M. F. Advances in multiscale modeling of lignocellulosic biomass. *ACS Sustainable Chem. Eng.* **2020**, *8*, 3512−3531.

(7) Bharadwaj, A.; Baxter, L. L.; Robinson, A. L. Effects of intraparticle heat and mass transfer on biomass devolatilization: experimental results and model predictions. *Energy Fuels* **2004**, *18*, 1021−1031.

(8) Park, W. C.; Atreya, A.; Baum, H. R. Experimental and theoretical investigation of heat and mass transfer processes during wood pyrolysis. *Combust. Flame* **2010**, *157*, 481−494.

(9) Caposciutti, G.; Almuina-Villar, H.; Dieguez-Alonso, A.; Gruber, T.; Kelz, J.; Desideri, U.; Hochenauer, C.; Scharler, R.; Anca-Couce, A. Experimental investigation on biomass shrinking and swelling behaviour: particles pyrolysis and wood logs combustion. *Biomass Bioenergy* **2019**, *123*, 1−13.

(10) Holmgren, P.; Wagner, D. R.; Strandberg, A.; Molinder, R.; Wiinikka, H.; Umeki, K.; Broström, M. Size, shape, and density changes of biomass particles during rapid devolatilization. *Fuel* **2017**, *206*, 342−351.

(11) Shen, J.; Wang, X.-S.; Garcia-Perez, M.; Mourant, D.; Rhodes, M. J.; Li, C.-Z. Effects of particle size on the fast pyrolysis of oil mallee woody biomass. *Fuel* **2009**, *88*, 1810−1817.

(12) Lu, H.; Robert, W.; Peirce, G.; Ripa, B.; Baxter, L. L. Comprehensive study of biomass particle combustion. *Energy Fuels* **2008**, *22*, 2826−2839.

(13) Ciesielski, P. N.; Crowley, M. F.; Nimlos, M. R.; Sanders, A. W.; Wiggins, G. M.; Robichaud, D.; Donohoe, B. S.; Foust, T. D. Biomass particle models with realistic morphology and resolved microstructure for simulations of intraparticle transport phenomena. *Energy Fuels* **2015**, *29*, 242−254.

(14) Pecha, M. B.; Thornburg, N. E.; Peterson, C. A.; Crowley, M. F.; Gao, X.; Lu, L.; Wiggins, G.; Brown, R. C.; Ciesielski, P. N. Impacts of anisotropic porosity on heat transfer and off-gassing during biomass pyrolysis. *Energy Fuels* **2021**, *35*, 20131−20141.

(15) Fatehi, H.; Bai, X.-S. A comprehensive mathematical model for biomass combustion. *Combust. Sci. Technol.* **2014**, *186*, 574−593.

(16) Paulsen, A. D.; Mettler, M. S.; Dauenhauer, P. J. The role of sample dimension and temperature in cellulose pyrolysis. *Energy Fuels* **2013**, *27*, 2126−2134.

(17) Fu, P.; Hu, S.; Xinag, J.; Sun, L.; Yang, T.; Zhang, A.; Wang, Y.; Chen, G. In *Effects of Pyrolysis Temperature on Characteristics of Porosity in Biomass Chars*, 2009 International Conference on Energy and Environment Technology, IEEE, 2009; pp 109−112.

(18) Haas, T. J.; Nimlos, M. R.; Donohoe, B. S. Real-time and post-reaction microscopic structural analysis of biomass undergoing pyrolysis. *Energy Fuels* **2009**, *23*, 3810−3817.

(19) Grønli, M. G.; Melaaen, M. C. Mathematical model for wood pyrolysis comparison of experimental measurements with model predictions. *Energy Fuels* **2000**, *14*, 791−800.

(20) Davidsson, K. O.; Pettersson, J. B. Birch wood particle shrinkage during rapid pyrolysis. *Fuel* **2002**, *81*, 263−270.

(21) Papadikis, K.; Gu, S.; Bridgwater, A. V. CFD modelling of the fast pyrolysis of biomass in fluidised bed reactors: modelling the impact of biomass shrinkage. *Chem. Eng. J.* **2009**, *149*, 417−427.

(22) Pyle, D.; Zaror, C. Heat transfer and kinetics in the low temperature pyrolysis of solids. *Chem. Eng. Sci.* **1984**, *39*, 147−158.

(23) Di Blasi, C. Heat, momentum and mass transport through a shrinking biomass particle exposed to thermal radiation. *Chem. Eng. Sci.* **1996**, *51*, 1121−1132.

(24) Beetham, S.; Capecelatro, J. Biomass pyrolysis in fully-developed turbulent riser flow. *Renewable Energy* **2019**, *140*, 751−760.

(25) Gentile, G.; Debiagi, P. E. A.; Cuoci, A.; Frassoldati, A.; Ranzi, E.; Faravelli, T. A computational framework for the pyrolysis of anisotropic biomass particles. *Chem. Eng. J.* **2017**, *321*, 458−473.

(26) Wang, W.; Lu, Y.; Xu, K.; Wu, K.; Zhang, Z.; Duan, J. Experimental and simulated study on fluidization characteristics of particle shrinkage in a multi-chamber fluidized bed for biomass fast pyrolysis. *Fuel Process. Technol.* **2021**, *216*, No. 106799.

(27) Chen, S.; Doolen, G. D. Lattice Boltzmann method for fluid flows. *Annu. Rev. Fluid Mech.* **1998**, *30*, 329−364.

(28) Xiong, Q.; Kong, S.-C. High-resolution particle-scale simulation of biomass pyrolysis. *ACS Sustainable Chem. Eng.* **2016**, *4*, 5456−5461.

(29) Pan, Y.; Kong, S.-C. Simulation of biomass particle evolution under pyrolysis conditions using lattice Boltzmann method. *Combust. Flame* **2017**, *178*, 21−34.

(30) Wang, J.; Wang, M.; Li, Z. A lattice Boltzmann algorithm for fluid−solid conjugate heat transfer. *Int. J. Therm. Sci.* **2007**, *46*, 228−234.

(31) Li, L.; Chen, C.; Mei, R.; Klausner, J. F. Conjugate heat and mass transfer in the lattice Boltzmann equation method. *Phys. Rev. E* **2014**, *89*, No. 043308.

(32) Seddiq, M.; Maerefat, M.; Mirzaei, M. Modeling of heat transfer at the fluid−solid interface by lattice Boltzmann method. *Int. J. Therm. Sci.* **2014**, *75*, 28−35.

(33) Karani, H.; Huber, C. Lattice Boltzmann formulation for conjugate heat transfer in heterogeneous media. *Phys. Rev. E* **2015**, *91*, No. 023304.

(34) Hu, Y.; Li, D.; Shu, S.; Niu, X. Full Eulerian lattice Boltzmann model for conjugate heat transfer. *Phys. Rev. E* **2015**, *92*, No. 063305.

(35) Rihab, H.; Moudhaffar, N.; Sassi, B. N.; Patrick, P. Enthalpic lattice Boltzmann formulation for unsteady heat conduction in heterogeneous media. *Int. J. Heat Mass Transfer* **2016**, *100*, 728−736.

(36) Hosseini, S. A.; Darabiha, N.; Thévenin, D. Lattice Boltzmann advection-diffusion model for conjugate heat transfer in heterogeneous media. *Int. J. Heat Mass Transfer* **2019**, *132*, 906−919.

(37) Gao, D.; Chen, Z.; Chen, L.; Zhang, D. A modified lattice Boltzmann model for conjugate heat transfer in porous media. *Int. J. Heat Mass Transfer* **2017**, *105*, 673−683.

(38) Liu, Q.; Feng, X.-B.; He, Y.-L.; Lu, C.-W.; Gu, Q.-H. Three-dimensional multiple-relaxation-time lattice Boltzmann models for single-phase and solid-liquid phase-change heat transfer in porous media at the REV scale. *Appl. Therm. Eng.* **2019**, *152*, 319−337.

(39) Krüger, T.; Kusumaatmaja, H.; Kuzmin, A.; Shardt, O.; Silva, G.; Viggen, E. M. *The Lattice Boltzmann Method*; Springer International Publishing, 2017; Vol. *10*, pp 4−15.

(40) He, X.; Chen, S.; Doolen, G. D. A novel thermal model for the lattice Boltzmann method in incompressible limit. *J. Comput. Phys.* **1998**, *146*, 282−300.

https://doi.org/10.1021/acs.energyfuels.2c03892
Energy Fuels 2023, 37, 5926−5941

(41) Chen, S.; Liu, Z.; Zhang, C.; He, Z.; Tian, Z.; Shi, B.; Zheng, C. A novel coupled lattice Boltzmann model for low Mach number combustion simulation. *Appl. Math. Comput.* **2007**, *193*, 266−284.
(42) Lei, T.; Wang, Z.; Luo, K. H. Study of pore-scale coke combustion in porous media using lattice Boltzmann method. *Combust. Flame* **2021**, *225*, 104−119.
(43) Li, Q.; Luo, K.; He, Y.; Gao, Y.; Tao, W. Coupling lattice Boltzmann model for simulation of thermal flows on standard lattices. *Phys. Rev. E* **2012**, *85*, No. 016710.
(44) Guo, Z.; Zheng, C.; Shi, B.; Zhao, T. Thermal lattice Boltzmann equation for low Mach number flows: Decoupling model. *Phys. Rev. E* **2007**, *75*, No. 036704.
(45) Liu, H.; Kang, Q.; Leonardi, C. R.; Schmieschek, S.; Narváez, A.; Jones, B. D.; Williams, J. R.; Valocchi, A. J.; Harting, J. Multiphase lattice Boltzmann simulations for porous media applications. *Comput. Geosci.* **2016**, *20*, 777−805.
(46) Nield, D. A.; Bejan, A. *Convection in Porous Media*; Springer, 2006.
(47) Guo, Z.; Zhao, T. Lattice Boltzmann model for incompressible flows through porous media. *Phys. Rev. E* **2002**, *66*, No. 036304.
(48) Guo, Z.; Zhao, T. A lattice Boltzmann model for convection heat transfer in porous media. *Numer. Heat Transfer, Part B* **2005**, *47*, 157−177.
(49) Yoshida, H.; Nagaoka, M. Multiple-relaxation-time lattice Boltzmann model for the convection and anisotropic diffusion equation. *J. Comput. Phys.* **2010**, *229*, 7774−7795.
(50) Debiagi, P.; Faravelli, T.; Hasse, C.; Ranzi, E. Kinetic Modeling of Solid, Liquid and Gas Biofuel Formation from Biomass Pyrolysis. In *Production of Biofuels and Chemicals with Pyrolysis*; Springer, 2020; pp 31−76.
(51) Dellar, P. J. An interpretation and derivation of the lattice Boltzmann method using Strang splitting. *Comput. Math. Appl.* **2013**, *65*, 129−141.
(52) Lallemand, P.; Luo, L.-S. Lattice Boltzmann equation with Overset method for moving objects in two-dimensional flows. *J. Comput. Phys.* **2020**, *407*, No. 109223.
(53) Yamamoto, K.; Takada, N.; Misawa, M. Combustion simulation with Lattice Boltzmann method in a three-dimensional porous structure. *Proc. Combust. Inst.* **2005**, *30*, 1509−1515.
(54) Premnath, K. N.; Abraham, J. Three-dimensional multi-relaxation time (MRT) lattice-Boltzmann models for multiphase flow. *J. Comput. Phys.* **2007**, *224*, 539−559.
(55) Hecht, M.; Harting, J. Implementation of on-site velocity boundary conditions for D3Q19 lattice Boltzmann simulations. *J. Stat. Mech.: Theory Exp.* **2010**, *2010*, No. P01018.
(56) Noble, D. R.; Torczynski, J. A lattice-Boltzmann method for partially saturated computational cells. *Int. J. Mod. Phys. C* **1998**, *9*, 1189−1201.
(57) Patankar, S. V. *Numerical Heat Transfer and Fluid Flow*; CRC Press, 2018.
(58) Stewart, R. B.; Jacobsen, R. T. Thermodynamic properties of argon from the triple point to 1200 K with pressures to 1000 MPa. *J. Phys. Chem. Ref. Data* **1989**, *18*, 639−798.
(59) Wałowski, G. Assessment of gas permeability coefficient of porous materials. *J. Sustain. Min.* **2017**, *16*, 55−65.
(60) Crowley, M. F.; Sitaraman, H.; Klinger, J.; Usseglio-Viretta, F.; Thornburg, N. E.; Brunhart-Lupo, N.; Pecha, M. B.; Dooley, J. H.; Xia, Y.; Ciesielski, P. N. Measurement of Transport Properties of Woody Biomass Feedstock Particles Before and After Pyrolysis by Numerical Analysis of X-Ray Tomographic Reconstructions. *Front. Energy Res.* **2022**, *10*, No. 850630.
(61) Richter, A.; Nikrityuk, P. A. Drag forces and heat transfer coefficients for spherical, cuboidal and ellipsoidal particles in cross flow at sub-critical Reynolds numbers. *Int. J. Heat Mass Transfer* **2012**, *55*, 1343−1354.
(62) Ranz, W. Evaporation from Drops-I and-II. *Chem. Eng. Prog.* **1952**, *48*, 173−180.

https://doi.org/10.1021/acs.energyfuels.2c03892
Energy Fuels 2023, 37, 5926−5941